Delineation of mineral potential zone using U-statistic method in processing satellite remote sensing images

Seyyed Saeed Ghannadpour [a, *], Samaneh Esmailzadeh Kalkhoran [a], Hadi Jalili [b] and Maedeh Behifar [b]

[a] *Department of Mining Engineering, Amirkabir University of Technology.*

[b] *Iranian Space Research Center, Tehran, Iran.*

ABSTRACT

Delineating and mapping alteration zones in porphyry copper exploration is of special importance. In this study, satellite image processing techniques were employed to highlight alteration zones in the Zafarghand exploration area. The Zafarghand area is located in the southeastern part of Ardestan and the northwestern part of Isfahan. It is situated within the geological structural zones of central Iran and the intermediate magmatic arc of Urmia-Dokhtar. Various alteration haloes are present in this area, including phyllic, potassic, propylitic, argillic, and slightly siliceous alterations. In this study, the detection of related alterations was carried out using ASTER sensor imagery. Accordingly, considering the raster nature and digital form of satellite images, the digital number values of each pixel from the image matrices were considered as samples in a systematic network. Finally, the U spatial statistic algorithm was implemented as a moving window algorithm for determining anomaly samples in the set of digital number (DN) values of ASTER satellite image pixels. The results of this technique show that the application of the U-statistic method, considering its structural nature and neighboring samples in decision-making, has been successful and has proven to be very effective in determining the alteration zones in the Zafarghand area. It could be observed the delineated propylitic alteration by the U-statistic method is closely associated with the defined zone of propylitic alteration, which is also consistent with the field and microscopic observation of the porphyry Cu mineralization in this alteration zone. It is also observed that the determined phyllic alteration by this image processing is spatially conformable with the sericitic alteration presented in the alteration map (based on field observations and geochemical sampling).

Keywords: *U statistic, Satellite image processing, ASTER, Zafarghand, Porphyry copper.*

1. Introduction

During the late twentieth century, the use of remote sensing technology became prevalent in identifying various ore deposits, including epithermal, porphyry, and volcanic massive sulfide deposits [1]. This technology proved to be a valuable tool in the initial stages of mineral exploration [2].

Remote sensing technology, which merges images and spectra [3], has rapidly gained popularity in the field of Earth observation [4]. Hyperspectral imaging systems with high spectral resolution are commonly used to scan observation areas with hundreds of continuous spectral bands simultaneously [5]. In remote sensing imagery, each pixel contains spectral information, which is added as a third dimension to a two-dimensional (2-D) image, creating a three-dimensional (3-D) cube [6]. These hyperspectral cubes contain absorption and reflectance spectral data for each pixel [7].

The demand for regional-scale mineral mapping has increased in the 21st century, leading many researchers to focus on mineral information extraction. Typically, this involves comparing an unknown spectrum to a reference spectrum in hyperspectral images [8]. Geologists rely on spectral characteristics as diagnostic features to identify and differentiate between various alteration types using remote sensing data. To extract information for mineral mapping, common remote sensing techniques rely on the diagnostic absorption characteristics, such as MTMF (mixture-tuned matched-filtering) [9], RBD (relative band depth) [10], BD (band ratio) [11] and SAM (spectral angle mapping) [12].

On the other, in mineral exploration, one of the most important tasks is mapping geochemical anomalies. In order to separate anomalous samples from the background and finally prepare geochemical anomaly maps, different statistical methods have been presented. One of the most important and effective of these methods is the U-statistic method [13-16]. This methos as a structural method, evaluates the sample under consideration by considering a moving window (based on the location and concentration of surrounding samples). By assigning a new value to each sample (instead of its concentration), the U-statistic method provides the ability to be combined with other methods [17-21].

Therefore, in this research, based on the aforementioned capability, it will be combined with the BD technique for the purpose of processing satellite images. In fact, this research focuses on processing satellite images from the ASTER sensor in order to identify surface alterations by employing the U-statistics method. Finally, the performance of this combined method will be investigated by the explorational data of copper porphyry in Zafarghand. The Zafarghand exploration area (in

---

northeastern Isfahan) is located in the central part of the Urmia-Dokhtar Magmatic Arc (UDMA) (Fig. 1) [22]. In recent years, numerous studies have been carried out in this area, which will be briefly described below.

The initial exploration activity in the region involved the preparation of a geological map with a scale of 1:5000, lithological sampling, and preparing geophysical sections in the area [25].

Subsequent geochemical and petrological studies have been conducted on volcanic and volcaniclastic rocks, as well as on neighboring or similar granitoid masses and andesite-basaltic dykes that cut across the Eocene volcanic rocks. These studies were carried out by [26-29]. In 2011, the petrogenesis of the Zafarghand granitoid mass was studied by Sadeghian and Ghafari [26].

Aminoroaya Yamini et al. studied the thermal alterations of this deposit with a focus on mineralogical and geochemical changes in 2016 [30]. Alaminia et al. also examined the geochemistry, geophysics, and fluids inclusions in this area in 2017 [22]. Aminoroaya Yamini et al. also investigated the evolution of the magmatic system in this deposit, considering plagioclase as an indicator [31].

In another study, the relationship between mineralization and alteration zones with tectonic structures was investigated by Mohammadi et al. emplying remote sensing studies [32].

In 2016, the chloritization of biotite was analyzed to study the mineralization parameters and associated alteration in the Zafarghand porphyry copper system, using mineral chemistry and stable isotope analysis [33].

Fig. 1. A: Display of the Zafarghand exploration area in the central section of the

UDMA and B: A part of the simplified Ardestan and Shahrab geological map with a scale of 1:100,000 (after slight modifications from [22-24]) (the location of Fig. 2 is also depicted in this figure).

Aminoroaya Yamini et al. also studied the petrography, geochemistry, and alteration thermometry of syno-sedimentary copper mineralization in this area [34]. The isotopic and geochemical constraints on the role of crust-magma mixing in the UDMA were determined, with a focus on the microgranular mafic enclaves and genetic granitoids in the igneous Zafarghand complex [35]. In 2017, the Zafarghand exploration area was considered a case study for identifying deep and blind mineral deposits using the newly proposed frequency coefficient method in the field of geochemical data [36].

2. Geological Setting of the Zafarghand Porphyry Copper System

The Zafarghand copper exploration area is located in southeastern Ardestan, in central Iran, about 110 kilometers northeast of Isfahan. The deposit is situated in the west of Zafarghand, within the 1:100,000 Ardestan geological sheet, ranging from 55°23'52"E to 30°26'52"E longitude and 52°11'33"N to 30°10'33"N latitude (Fig. 2) [22]. To access the area, one can use the Ardestan-Naeen road in the western part, Ardestan-Isfahan road in the central section, Zafarghand-Zefreh road in the southern part, and Ardestan-Natanz road in the northern part of the region. The studied deposit is located in the western margin of the Central Iran structural zone and in the central part of the UDMA, similar to other porphyry copper deposits in Iran and worldwide, it has a magmatic origin.
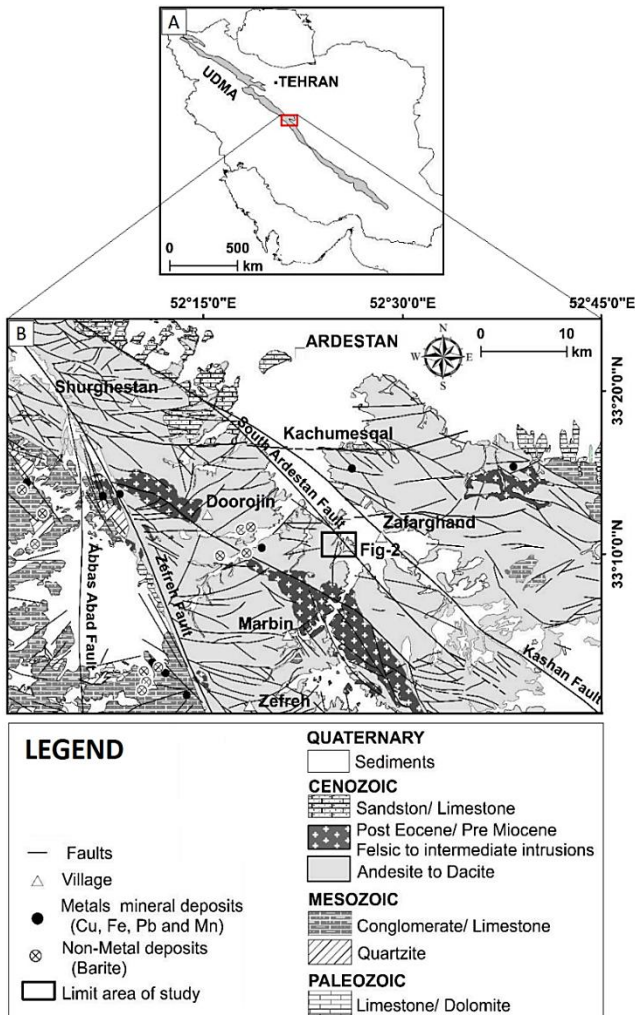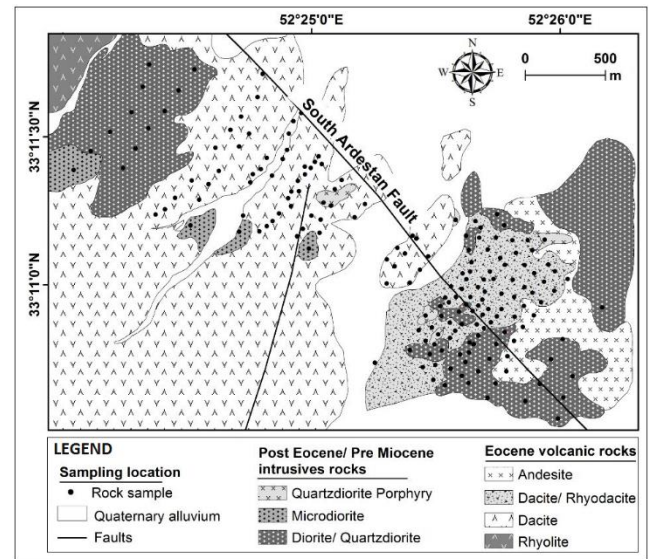

Fig. 2. The simplified geological map of the Zafarghand exploration area (modified after [22]).

Based on field investigations and petrography carried out in this area, acidic to intermediate igneous rocks, including volcanic and intrusive rocks belonging to the upper Eocene and younger time period, are outcrops, which are described in the following rock units [22]. Rhyolite has a relatively small outcrop in the northwest corner with a pinkish gray color (Fig. 2). The texture of these rocks is porphyritic with a glassy flow. Dacites and rhyodacites cover a wide range of the area and have gray to greenish colors (Fig. 2). This unit is considered the most important host rock for copper mineralization in the region, and has a porphyry texture with fine-grained, amorphous and porous felsic paste. Andesites are relatively large in the southwestern and western parts of the region (Fig. 2), and they appear dark gray and they are hollow due to the abundance of coarse crystals. Intrusive masses of diorite, quartz diorite, and micro-diorite protrude in the northwestern and southeastern parts of the region with a dark gray color (Fig. 2). A semi-

intrusive porphyritic quartz diorite mass covers a small area in the southeastern part of the region (Fig. 2) [22].

2.1. Alteration and mineralization

Based on the conducted studies and investigations, the different alterations in the region include potassic, phyllic, siliceous, argillic, and propylitic alterations. These alterations are often observed near intrusive masses and host rocks around the South Ardestan fault (Fig. 3) [22]. In the southeastern corner of the area, potassic alteration is very limited near the quartz diorite mass, while phyllic alteration is observed near the intrusive diorite and porphyritic quartz diorite masses, as well as the dacite and rhyodacite volcanic rocks. Siliceous and argillic alterations have limited replacement of phyllic alteration (Fig. 3). Propylitic alteration is widespread in the outer area of the deposit (Fig. 3) [22]. It should be noted that chlorite is observed in a wide area of the south Ardestan region.
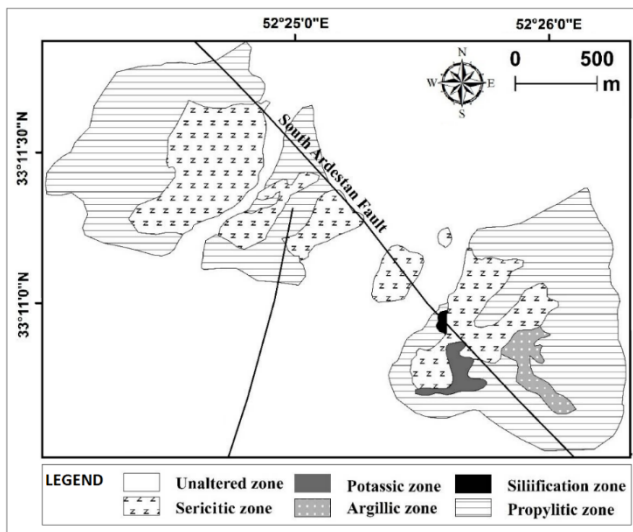

Fig. 3. Expansion of halo effects in the Zafarghand exploration area (modified after [22]).

3. Material and Method

3.1. Data

In line with the main objective of this study and for highlighting various geological anomalies and important indicator minerals in the assessment of mineral potential in the study area, ASTER satellite images will be utilized.

The ASTER (Advanced Spaceborne Thermal Emission and Reflection Radiometer) sensor is mounted on the Terra satellite and was launched into space in 1999. The data from this sensor consists of 14 bands as shown in Table 1 [37], with three bands in the VNIR range with a spatial resolution of 15 meters, six bands in the SWIR range with a spatial resolution of 30 meters, and five bands in the TIR range with a spatial resolution of 90 meters. Each ASTER image covers an area of 60×60 square kilometers. Due to the multiple bands in the SWIR and TIR ranges, ASTER images have extensive applications in geological studies, particularly in the identification of alteration zones. The SWIR bands of these images cover the absorption ranges of Al-O-H, Si-O-H, and Mg-O-H and could be effective in their identification [38]. Among the reflected infrared bands, six bands are designed in the wavelength range of 1.3 to 3.1 micrometers, which are very useful for geological applications (especially mineralogy). The five thermal infrared bands are also used for accurate estimation of surface temperature and measurement of various phenomena. In terms of radiometry, the reflected visible and infrared images are designed as 8-bit and the thermal infrared images are designed as 12-bit, which allows for increased radiometric accuracy of the thermal bands [39]. ASTER

sensor data are used to identify alteration zones, minerals, and lithology in geological studies. ASTER data, either alone or in combination with other remote sensing satellites and ground data, are used to produce geological maps [40]. ASTER has the capability of being combined with other remote sensing satellites as well. By combining ASTER data with other satellites and sensors, maps with higher accuracy could be generated. In many recent studies, the emphasis has been on the combined use of ASTER data and other remote sensing satellites. The most prominent example of this combination could be seen in Landsat and ASTER data.

The images employed in this study are L1T images for the year 2002, which were chosen because starting from 2008, the 6-band shortwave infrared (SWIR) detector of the ASTER sensor has been completely out of use and its data since then are provided without these mentioned bands on the sites. The use of the 4-band VNIR range of the Landsat sensor is suitable for intermediate metal, especially iron, rare Earth elements, and chlorophyll absorption in plants. While the 5-band coverage of the ASTER sensor compared to the 2-band wide Landsat range in the SWIR range has made it possible to distinguish hydroxyl group minerals, hydrates, carbonates, and most importantly, indicative minerals of feldspar, argillaceous, propylitic zones from each other.

3.2. U-statistic

The U spatial statistic method is considered an effective and powerful method in the field of separating geochemical anomalies. In fact, the basis of this method is a type of moving average, with the feature that the size of the window in which the averaging takes place changes at each specific point. Therefore, for each specific point, different values are calculated to determine the value of U, based on the surrounding points. In this way, at first, a distance criterion is determined in order to determine the distance and proximity of the sample. Then, a specific weight is assigned to each sample based on this measure, and the weighted average value of the points within the search range is calculated to determine their spread for each sample. Finally, the value of U is calculated using the following formula [13-14, 41-42].

$$U_i(r) = \frac{\bar{x}_i(r) - \mu}{\sigma} \tag{2}$$

In which μ is the average, r is the neighborhood radius, $x_i(r)$ is the weighted average value of the i-th sample, and σ is the standard deviation of the entire data. The value of $U_i(r)$ is a function of r, meaning that different values for U_i are obtained by changing r. For each r, a number of surrounding samples participate in calculating the value of U for the unknown point. As a result, different U values are obtained for the unknown point, and the highest value (regardless of its sign) is assigned to the sample (considering its sign). One of the advantages of the U-statistic method is its ability to be combined with other methods because this method assigns a new value to the samples. Using this new value (calculated U values), it could be combined with other methods to increase the efficiency of separation [17-21, 43-44].

Continuing in the results and discussion section, after performing the necessary preprocessing on the satellite images of the ASTER and data preparation, the U spatial statistic algorithm will be applied to the brightness values of each pixel, considering their coordinates. Finally, for enhancing the desired features, the band ratio method will be employed. Fig. 4. illustrates the steps of this study in the form of a flowchart.

4. Results and discussion

4.1. Preprocessing of satellite images

In this section, before applying the anomaly structural separation method, the preparation and preprocessing of satellite images will be discussed. Because in order to obtain information from satellite images, radiometric and geometric preprocessing is necessary before using them. Preprocessing includes operations that need to be done before the main data analysis and information extraction. Geometric and radiometric corrections are among these operations. Geometric

Table 1. General specifications of the ASTER sensor [37].

Subsystem	Band No.	Spectral Rang (m)	Spatial Resolutions (m)	Quantization Levels
VNIR	1	0.52-0.60	15	8 bits
	2	0.63-0.69		
	3 (N & B)	0.78-0.86		
SWIR	4	1.60-1.70	30	8 bits
	5	2.145-2.185		
	6	2.185-2.225		
	7	2.235-2.285		
	8	2.295-2.365		
	9	2.360-2.430		
TIR	10	8.125-8.475	90	12 bits
	11	8.475-8.825		
	12	8.925-9.275		
	13	10.25-10.95		
	14	10.95-11.65		
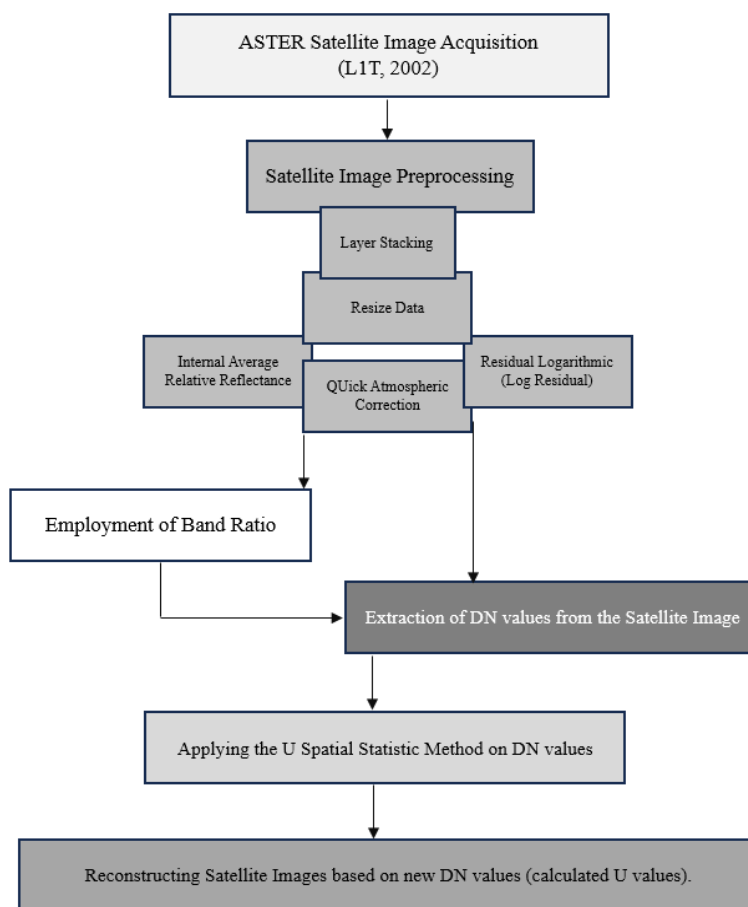
Fig. 4. The flowchart of various stages and the process of task execution.

corrections are performed to georeference the image, and radiometric corrections include actions to remove effects such as sunlight passing through clouds, suspended particles in space, oxygen, nitrogen, and other elements that create noise. In other words, radiometric corrections remove the factors that have affected the received spectra and create contrast in the received images. In this study, geometric correction has already been performed on the desired data, and these data have been georeferenced [45-47]. Only radiometric correction needs to be done on these data [45-47]. To eliminate the effects related to solar radiation, atmospheric transmission, and device errors, the residual logarithmic (Log Residual) method has been used to consider the topographic effects in ASTER images [48]. Moreover, the Internal Average Relative

Reflectance (IARR) method is suitable for dry and semi-arid areas due to their sparse vegetation cover and low water vapor as well as suitable atmospheric conditions. It is also effective for areas where no specific ground measurements are available [48]. The QUick Atmospheric Correction (QUAC) method has been employed to eliminate the effects of absorption and scattering of electromagnetic waves. This method is an atmospheric correction method for the visible, near-infrared, and mid-infrared ranges. This method is applicable for correcting multi-spectral and hyperspectral images in the range of 400 to 3000 nanometers. This algorithm is suitable for correcting images that have been previously prepared or images that do not have atmospheric and ground samples for the absolute method application [49].

4.2. Preparing satellite images for data extraction

After applying the aforementioned methods for image preprocessing of the Zafarghand region, in order to prepare the desired image for applying the U-statistic algorithm, the selected region of interest image was resized and bands 4 to 9 of the SWIR range were selected to extract the digital number (DN) values for each selected pixel. The selection of these bands was based on studies conducted on porphyry copper deposits with ASTER data for their employing in the band ratio method. These bands are considered the most important satellite image bands for enhancing the anomalies of porphyry copper deposits due to their absorption and reflectance characteristics. The resized output of bands 4 to 9 of the SWIR can be seen in Fig. 5. as an example. As observed, the quality of the desired image is not very high, which is due to the small size of the study area compared to a scene of ASTER satellite images

and the consequent decrease in the number of pixels. However, this issue not only did not create a problem during the course of this research, but the visibility of pixels in this image also indicates a distinct sample with known coordinates for applying the U-statistic method and displaying the impact of these methods on the data (DN values of each pixel).

The statistical specifications required for implementing the U-statistic method algorithm regarding the DN values for bands 4 to 9 in the SWIR range and the frequency distribution graph of DN values can be observed in Table 2 and Fig. 6, respectively.

As can be seen in Fig. 6, the values of DN follow a normal distribution. Therefore, there is no limitation in using the U-statistic method, which assumes normality of the data [50-51].
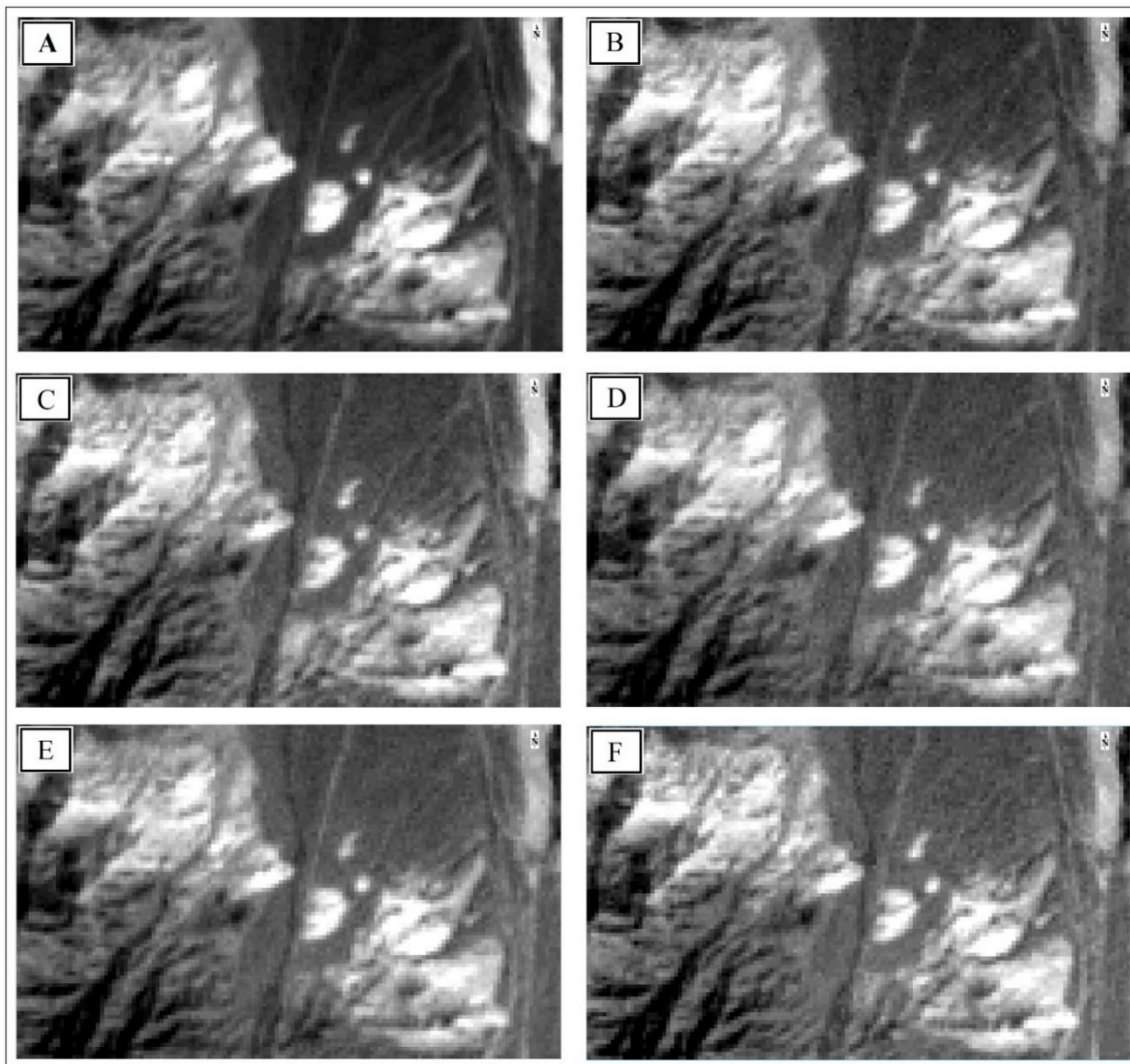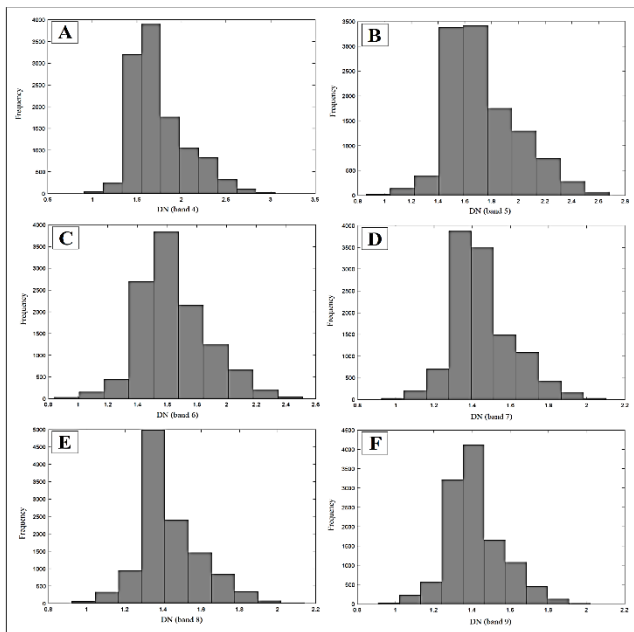

Fig. 5. Resized ASTER satellite images for the SWIR range in the Zafarghand region. A: Band 4, B: Band 5, C: Band 6, D: Band 7, F: Band 8, and E: Band 9.

Table 2: DN statistical specifications of the SWIR range bands (bands 4 to 9).

Band	Average	Variance	Standard deviation
4	1.7193	0.0988	0.3143
5	1.7164	0.0708	0.2660
6	1.6378	0.0551	0.2348
7	1.4454	0.0256	0.1601
8	1.4314	0.0279	0.1671
9	1.4126	0.0219	0.1481

Fig. 6. The histogram of DN values for the SWIR range. A: Band 4, B: Band 5, C: Band 6, D: Band 7, F: Band 8, and E: Band 9.

4.3. Applying the U spatial statistics algorithm to DN values

In this section, after extracting the DN values of each pixel from the set of image matrix, the desired values, similar to the samples' concentration related to a systematic dataset (geochemical data), along with their initial statistical characteristics and coordinates, are provided as input to the U spatial statistical method. Considering the spatial resolution of 30 meters for the SWIR range, both the initial radius value and its incremental value are set to 18 meters.

After applying the U statistical algorithm to the DN values of bands 4 to 9 in the SWIR range, the new DN values (i.e., the calculated U values for each pixel based on the DN values of the surrounding pixels) are computed. The statistical characteristics of the calculated U values as the new DN values, and their histogram can be observed in Table 3 and Fig. 7, respectively.

As can be observed in Fig. 7, the U values of each pixel, or in other words, the new DN values of the image matrix, are well separated from each other at the U=0 point. In fact, based on this, pixels with higher values are distinguished from those with lower values.

The calculated U values have replaced the previous DN values in the image matrix of the SWIR range (bounds 4 to 9), and the obtained results are displayed in Fig. 8.

As can be seen in the above images (Fig. 8), the anomalous values are well separated from the background values, and the desired objective is much clearer in the images than in Fig. 5. In this figure, the superiority of images with the U values compared to the initial values of the DN can be observed.

### 4.4. Enhancement of anomalies using Band Ratio technique

The Band Ratio (BR) method is one of the common techniques in the satellite image processing. Band ratioing could be used to enhance the spectral difference between bands and eliminate the effects of variations in shadow and brightness caused by topography [52]. By understanding the spectral properties of phenomena based on their spectral signatures, various phenomena, such as lithological unit boundaries and anomalies can be highlighted using this method.

In this method, the band with higher reflectance from the target is placed in the numerator, while the band with higher absorption for the same target is placed in the denominator. Since argillic-bearing

alteration zones have maximum absorption in bands 5 and 6 and maximum reflectance in bands 4 and 7, the argillic band ratio have used: $\frac{b_4+b_7}{b_5+b_6}$. For highlighting phyllic-bearing zones, considering the maximum absorption in band 6 and maximum reflectance in band 7, the phyllic band ratio have used: $\frac{b_7}{b_6}$. Similarly, for detecting propylitic-bearing zones, the propylitic band ratio have used: $\frac{b_6+b_9}{b_7+b_8}$ based on the reflectance characteristics in bands 6 and 9, and the absorption characteristics in bands 7 and 8 [53-56]. Images containing the calculated U values are prepared using three band ratios [57-59]: phyllic ratio: $\frac{b_7}{b_6}$, propylitic ratio: $\frac{b_6+b_9}{b_7+b_8}$ and argillic ratio: $\frac{b_4+b_7}{b_5+b_6}$, respectively for phyllic, propylitic and argillic alterations (Fig. 9).

As can be seen in the above figure (Fig. 9), the propylitic alteration identified based on the values of U (Fig. 9-B) is well correlated with the propylitic alteration shown in Fig. 3 (to better display this matter, the green dashed lines in part B of Fig. 10 and part C of it can be observed). Additionally, the phyllic alteration in Fig. 9-A is approximately consistent with the sericitic alteration presented in Fig. 3. The red dashed lines in part A of Fig. 10 better show this issue.

Furthermore, it should be noted that due to the very small extent of argillic alteration in the area (according to Fig. 3), the specific range of interest is not clearly and prominently shown in the image of Fig. 9-C.
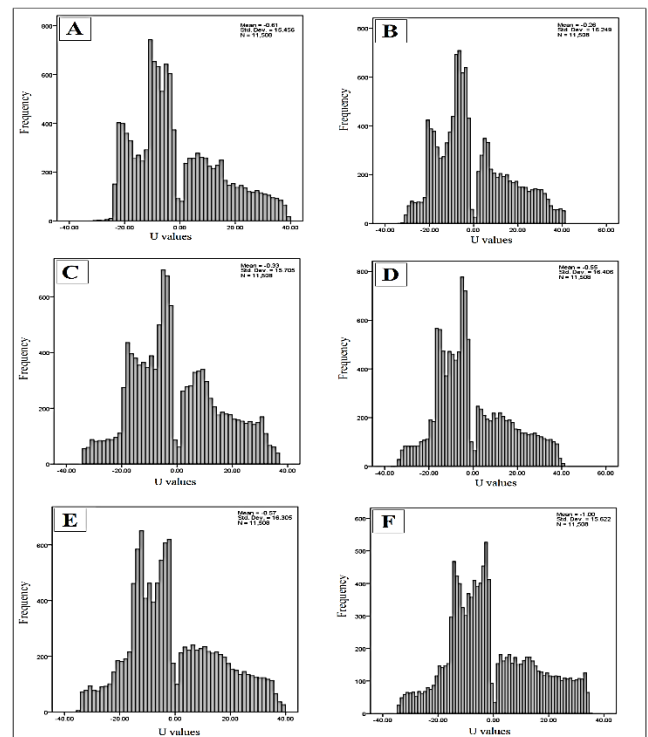

Fig. 7. The histogram of the calculated U values for the SWIR range. A: Band 4, B: Band 5, C: Band 6, D: Band 7, F: Band 8, and E: Band 9.

Table 3. U values statistical specifications of the SWIR range bands (bands 4 to 9).

Band	Average	Minium	Maximum
4	-0.60512	-33.8226	39.05852
5	-0.25911	-33.5285	41.28934
6	-0.33465	-34.0763	36.55587
7	-0.55412	-36.6264	40.62467
8	-0.57232	-37.1668	39.77979
9	-0.99509	-34.2129	34.74124
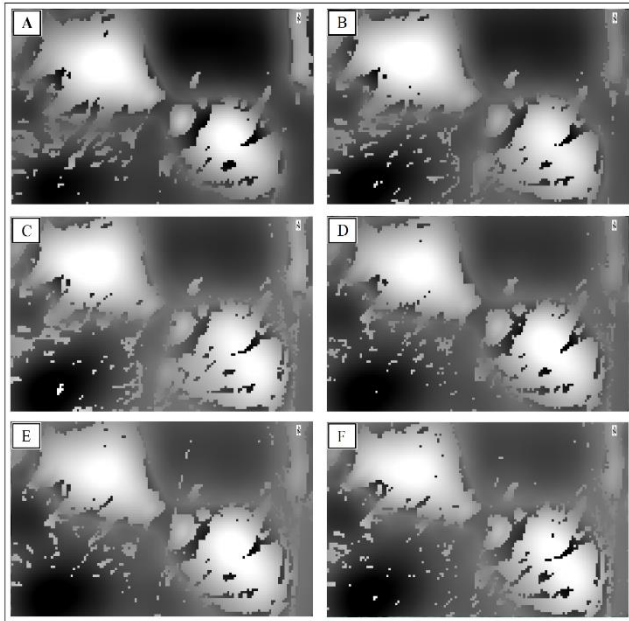
Fig. 8. ASTER satellite images with new DN values (calculated U values). A: Band 4, B: Band 5, C: Band 6, D: Band 7, F: Band 8, and E: Band 9.
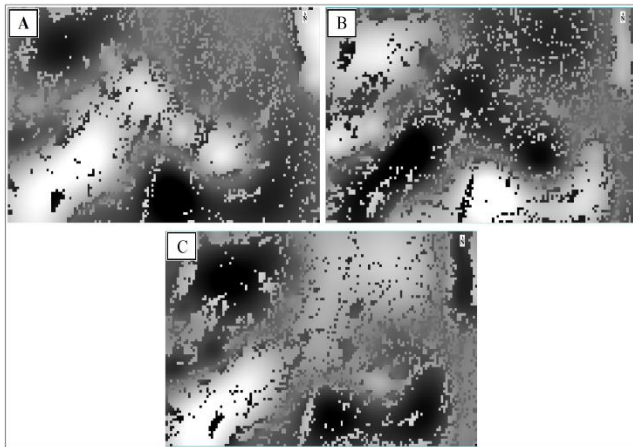
Fig. 9. ASTER satellite images with new DN values (the calculated U values). A: Phyllic Ratio: b_7/b_6 , B: Propylitic Ratio: (b_6+b_9)/(b_7+b_8) 5, C: Argillic Ratio: (b_4+b_7)/(b_5+b_6).
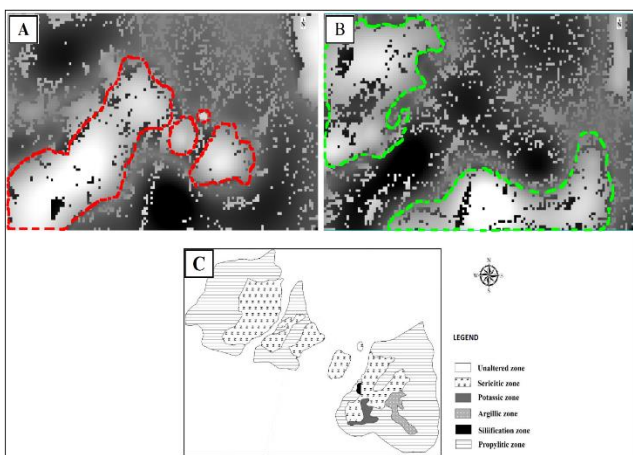
Fig. 10. Showing the phyllic propylitic alteration and their correspondence with the regional alteration map. A: Phyllic alteration by the red dashed line, B: Propylitic alteration by the green dashed line.

It is worth mentioning that the identified alterations in the southern region and their inconsistency with the map shown in Fig. 3 (or part C of Fig. 10) indicate the lack of geochemical sampling from the southern area. The alteration map depicted in Fig. 3 (or part C of Fig. 10) is based on geochemical sampling from the region. The sampling network of the Zafarghand exploration area can be seen in Fig. 2. and due to the absence of a sampling network design in the Zafarghand exploration zone's southern area, the alterations in the southern region are not represented in this map.

Phyllic and propylitic alterations are among the most important observations and exploration keys for porphyry copper deposits. The technique proposed in this research could be considered a powerful tool in the processing of satellite images, especially in the exploration of hydrothermal deposits, by showing the appropriate performance in the determination of these two alterations in the Zafarghand region.

5. Conclusion

In this study, the application of the U spatial statistic method, as a structural approach for separating anomalous values from the background, was employed to process satellite images (ASTER sensor imagery) and highlight the alterations of porphyry copper in the Zafarghand exploration zone in the northwest of Isfahan province. Considering the raster and digital nature of satellite images, and consequently, the existence of a regular matrix of DN values for each image, the U-statistic encounters a dataset similar to systematic data (similar to geochemical data). Based on the structural nature of the U-statistic method for separating anomalous values, the use of this method was very effective in processing raster-based satellite images. As can be observed in the results, the newly calculated values for each pixel as U values, determined based on the surrounding DN values, are far more suitable than the initial values of each pixel in the image matrix set. Furthermore, it was observed that the results of the band ratio enhancement method based on U values in the image matrix set show good conformity with the studied area's alterations. Results show (based on Fig. 10) that the delineated the propylitic alteration by the U-statistic method (Fig. 9-B and Fig. 10-B) is closely associated with the defined zone of propylitic alteration (Fig. 3 and Fig. 10-C), which is also consistent with the field and microscopic observations of the porphyry Cu mineralization in this alteration zone. It is also observed in Fig. 10 that the determined phyllic alteration by this image processing (Fig. 9-A and Fig. 10-A) is spatially conformable with the sericitic alteration presented in the alteration map (Fig. 3 and Fig. 10-C) (based on field observations and geochemical sampling).

REFERENCES

[1] Fu, Y., Cheng, Q., Jing, L., Ye, B., & Fu, H. (2023) Mineral Prospectivity Mapping of Porphyry Copper Deposits Based on Remote Sensing Imagery and Geochemical Data in the Duolong Ore District, Tibet. Remote Sensing. 15(2):439.

[2] Ranjbar, H., Honarmand, M., & Moezifar, Z. (2004). Application of the Crosta technique for porphyry copper alteration mapping, using ETM+ data in the southern part of the Iranian volcanic sedimentary belt. Journal Asian Earth Science. 2004, 24, 237–243.

[3] Xu, Q. Jin, W. Q., & Fu, L. Q. (2007). Calibration of the detection performance for hyperspectral imager. Guang Pu Xue Yu Guang Pu Fen Xi. 27, 1676–1679.

[4] Ghamisi, P., Yokoya, N., Li, J., Liao, W., Liu, S., Plaza, J., Rasti, B., & Plaza, A. (2017). Advances in hyperspectral image and signal processing: A comprehensive overview of the state of the art. IEEE Geosci. Remote Sens. Mag. 5, 37–78.

[5] Lee, H. S., Younan, N. H., & King, R. L. (2002). Hyperspectral image cube compression combining JPEG-2000 and spectral decorrelation. In Proceedings of the IEEE International

Geoscience and Remote Sensing Symposium, Toronto, ON, USA, 24–28 June 2002; IEEE: New York, NY, USA; pp. 3317–3319.

[6] Vasefi, F., MacKinnon, N., & Farkas, D. L. (2016). Chapter 16— Hyperspectral and multispectral imaging in dermatology. In Imaging in Dermatology; Hamblin, M.R., Avci, P., Gupta, G.K., Eds.; Academic Press: Boston, MA, USA; pp. 187–201.

[7] Lu, G., & Fei, B. (2014) Medical hyperspectral imaging: A review. J. Biomed. Opt. 19, 10901.

[8] Adams, J. B., & Gillespie, A. R. (2006). Remote Sensing of Landscapes with Spectral Images: A Physical Modeling Approach; Cambridge University Press: Cambridge, UK.

[9] Boardman, J. W., Kruse, F. A., & Green, R. O. (1995). Mapping target signatures via partial unmixing of AVIRIS data: In Summaries, Proceedings of the Fifth JPL Airborne Earth Science Workshop, Pasadena, CA, USA, 23–26 January 1995; SCISPACE: Bangalore, India; pp. 95–101.

[10] Crowley, J. K., Brickey, D. W., & Rowan, L. C. (1989). Airborne imaging spectrometer data of the Ruby Mountains, Montana: Mineral discrimination using relative absorption band-depth images. Remote Sens. Environ. 29, 121–134.

[11] Rowan, L. C., Goetz, A. F. H., & Ashley, R. P. (1977). Discrimination of hydrothermally altered and unaltered rocks in visible and near infrared multispectral images. Geophysics. 42, 522–535.

[12] Yuhas, R. H., Goetz, A. F. H., & Boardman, J. W. (1992). Discrimination among semi-arid landscape endmembers using the Spectral Angle Mapper (SAM) algorithm. In Proceedings of the Summaries of 3rd Annual JPL Airborne Geoscience Workshop, Pasadena, CA, USA, 1–5 June 1992; NTRS: Chicago, IL, USA; pp. 92–106.

[13] Ghannadpour, S. S., & Hezarkhani, A. (2016). Introducing 3D U-statistic method for separating anomaly from background in exploration geochemical data with associated software development. Journal of Earth System Science. 125(2), 387–401.

[14] Ghannadpour, S. S., Hezarkhani, A., Maghsoudi, A., & Farahbakhsh, E. (2015). Assessment of prospective areas for providing the geochemical anomaly maps of lead and zinc in Parkam district, Kerman, Iran. Geosciences Journal, 19(3), 431–440.

[15] Ghannadpour, S. S., & Hezarkhani, A. (2022). Prospecting rare earth elements (REEs) using radiation measurement: case study of Baghak mine, Central Sangan iron ore mine, NE of Iran. Environmental Earth Sciences. 81(14), 363.

[16] Ghannadpour, S. S., Hezarkhani, A., & Golmohammadi, A. (2018). Applying 3D U-statistic method for modeling the iron mineralization in Baghak mine, central section of Sangan iron mines. Geosystem Engineering. 21(5), 262-272.

[17] Ghannadpour, S. S., & Hezarkhani, A. (2022). A new method for determining geochemical anomalies: UN and UA fractal models. International Journal of Mining & Geo-Engineering. 56(2), 181-190.

[18] Ghannadpour, S. S., & Hezarkhani, A. (2022). Delineation of geochemical anomalies for mineral exploration using combining U-statistic method and fractal technique: UN and UA models. Applied Earth Science. 131(1), 32-40.

[19] Ghannadpour, S. S., Hezarkhani, A. Sharifzadeh, M., & Ghashghaei, F. (2019). Applying a structural multivariate method using the combination of statistical methods for the delineation of geochemical anomalies. Iranian Journal of

Science and Technology, Transactions A: Science. 43, 127-140.

[20] Ghannadpour, S. S., Hezarkhani, A., & Roodpeyma, T. (2017). Combination of Separation Methods and Data Mining Techniques for Prediction of Anomalous Areas in Susanvar, Central Iran. African Journal of Earth Sciences, 134, 516–525.

[21] Ghannadpour, S. S., & Hezarkhani, A. (2018). Providing the bivariate anomaly map of Cu–Mo and Pb–Zn using combination of statistic methods in Parkam district, Iran. Carbonates and Evaporites, 33(3), 403-420.

[22] Alaminia, A., Bagheri, H., & Salehi, M. (2017). Geochemical and geophysical investigations, and fluid inclusion studies in the exploration area of Zafarghand (Northeast Isfahan, Iran). Journal of Economic Geology, 9(2), 295-312. (In Persian with English Abstract)

[23] Radfar, J. (1998). Geological map of Ardestan, scale 1:100,000. Geological Survey of Iran, Tehran, Iran.

[24] Bahroudi, A. (2000). Geological map of Shahrab, scale 1:100,000. Geological Survey of Iran, Tehran, Iran.

[25] ANJC (Alamut Naghsh-e-Jahan Company), (2011). Initial exploration report of Zafarghand copper index, Isfahan, Iran, 270 pp. (in Persian)

[26] Sadeghian, M., & Ghaffary, M. (2011). The petrogenesis of Zafarghand granitoid pluton (SE of Ardestan). Petrology, 6, 47-70. (In Persian with English Abstract)

[27] Amidi, S. M. (1975). Contribution a Í etude stratigraphique, pétrologique et pétrochimique des roches magmatiques de la région Natanz-Nain-Surk (Iran Central). These université scientifique et médicale de Grenoble, France.

[28] Zahedi, M. & Amidi, S. M. (1975). 1:250000 geological map of Kashan. Geological Surevy of Iran, Tehran, Iran.

[29] Radfar, J., Alaee-Mahabadi, S., & Emami, M.H. (1993). Geological map of Kashan, scale 1:100000.Geological Survey of Iran, Tehran, Iran.

[30] Aminroayaei Yamini, M., Tutti, F., & Ahmadian, J. (2016). Geochemical and mineralogical evolution of the porphyry copper deposit in southwestern Zafarqand with emphasis on hydrothermal alteration. Researches in Earth Sciences, 7(1), 75-90. (In Persian with English Abstract)

[31] Aminroayaei Yamini, M., Tutti, F., Aminoroayaei Yamini, M. & Ahmadian, J. (2018). Plagioclase as evidence of magmatic evolution in the Zafarqand porphyry copper deposit, NE Isfahan. Journal of Economic Geology, 10(1), 61-76. (In Persian with English Abstract)

[32] Mohammadi, S., Nadimi, A., & Alaminia, Z. (2018). Archive of SIDAnalysis of the relationship between mineralization and alteration zones with tectonic s tructures using remote sensing studies in south Ardestan area (northeastern Isfahan). Tectonics, 7: 29-47. (In Persian with English Abstract)

[33] Aminoroayaei Yamini, M., Tutti, F., Haschke, M., Ahmadian, j., & Murata, M. (2016). Synorogenic copper mineralization during the Alpine–Himalayan orogeny in the Zafarghand copper exploration district, Central Iran: petrogrography, geochemistry and alteration thermometry. Geological Journal, 25(2): 263-281.

[34] Aminoroayaei Yamini, M., Tutti, F., & Aminoroayaei Yamini, M. (2017). Examination of chloritization of biotite as a tool for reconstructing the physicochemical parameters of mineralization and associated alteration in the Zafarghand porphyry copper system, Ardestan, Central Iran: mineral-chemistry and stable isotope analyses. Mineralogy and

Petrology, 111, 747-759.

[35] Sarjoughian, F., Lentz, D., Kananian, A., Ao, S., & Xiao, W. (2018). Geochemical and isotopic constraints on the role of juvenile crust and magma mixing in the UDMA magmatism, Iran: evidence from mafic microgranular enclaves and cogenetic granitoids in the Zafarghand igneous complex. International Journal of Earth Sciences, 107, 1127-1151.

[36] Shahi, H., Ghavami, R., & Kamkar Rouhani, A. (2016). Detection of deep and blind mineral deposits using new proposed frequency coefficients method in frequency domain of geochemical data. Journal of Geochemical Exploration, 169, 29-39.

[37] Biranvandpour, A., & Hashim, M. (2014). ASTER, ALI and Hyperion sensors data for lithological mapping and ore minerals exploration. Springer Plus, 3,130.

[38] Li, Q., Zhang, B., Lu, L., & Lin, Q. (2014). Hydrothermal alteration mapping using ASTER data in Baogutu porphyry deposit, China, in: IOP Conference Series: Earth and Environmental Science. IOP Publishing, p. 012174.

[39] Geotz, A., Billingsley, F., Elston, D., Lucchitta, I., Shoemaker, E., Abrams, M., Gillespie, A., Squries, R. (1975). Applications of ERTS Image and Image Procrssing to Regional Problems and Geologic Mapping in Northern Arizona. NASA/JPL Thechnical Reports 32-1597, NASA: Pasadena, CA, USA.

[40] Plafcan, D. (2011). Technoscientific Diplomacy: The practice of international policies in the ASTER collaboration, In Land Remote Sensing and Global Environmental Change. Ramachandran, R., Justice, C., Abrams, M., Eds., Springer: New York, NY, USA; Chapter4, 483-508.

[41] Ghannadpour, S. S., & Hezarkhani, A. (2017). Comparing U-statistic and nonstructural methods for separating anomaly and generating geochemical anomaly maps of Cu and Mo in Parkam district, Kerman, Iran. Carbonates and Evaporites, 32(3), 155-166.

[42] Ghannadpour, S. S., Hezarkhani, A., & Sabetmobarhan A. (2017). The Parkam exploration district (Kerman, Iran): Geology, alterations, and delineation of Cu- and Mo-mineralized zones using U-spatial statistic with associated software development. Journal of Earth Sciences. 28(2), 283–294.

[43] Ghannadpour, S. S., Hezarkhani, A., & Sharifzadeh, M. (2017). A method for extracting anomaly map of Au and As using combination of U-statistic and Euclidean distance methods in Susanvar district, Iran. Journal of Central South University, 24(11), 2693–2704.

[44] Ghannadpour, S. S., & Hezarkhani, A. (2020). Mineral potential mapping for Au and As using Gap statistic method in multivariate mode. Carbonates and Evaporites, 35(1), 1-11. https://doi.org/10.1007/s13146-019-00546-8

[45] Beiranvand Pour, A., & Hashim, M. (2011). Identification of hydrothermal alteration mineral for exploration of porphyry copper deposit using ASTER data, SE Iran. ELSEVER: Journal of Asian Earth Sciences, 42, 1309-1323.

[46] Oleson, R., & Doescher, Ch. (2022). Advance Spaceborne Thermal Emission and Reflection Radiometer (ASTER) Level 1 Precisin Terrain Corrected Registered At-sensor Radiance Product (AST_L1T). Department of the Interior U.S Geological Survey, Page 16.

[47] Abubakar, A. J., Hashim, M., & Beiranvand Pour, A. (2019). Remote Sensing satellite imagery for prospecting geothermal systems in an aseismic geologic setting: Yankari Park, Nigeria.

ELSEVIER: Int J AppL ObS Geoinformation, 80, 157-172.

[48] Fereydooni, H., & Mojeddifar, S. (2023). A directed matvhed filtering algorithm (DMF) for discriminating hydrothermal alteration zones using the ASTER remote sensing data. ELSEVIER: Int J Appl Earth Obs Geoinformation, 63, 1-13.

[49] Bernstein, L. S., Adler-Golden, S. M., Sundberg, R. L., Levine, & R. Y. (2005), Validation of the QUAC Atmospheric Correction (QUAC) algorithm for VNIR-SWIR multi- and hyperspectral imagery, SPIE Proceedings. Algorithm and Technologies for Multispectral, Hyperspectral and Ultraspacectral Imagery XI, 5806, 668-678.

[50] Ghannadpour, S. S., & Hezarkhani, A. (2015). Lead and zinc geochemical behavior based on geological characteristics in Parkam Porphyry Copper System, Kerman, Iran. Journal of Central South University, 22, 4274-4290.

[51] Ghannadpour, S. S., Hezarkhani, A., & Sabetmobarhan A. (2015). Some statistical analyses of Cu and Mo variates and geological interpretations for Parkam porphyry copper system, Kerman, Iran. Arabian Journal of Geosciences. 8, 345-355.

[52] Hewson, R. D., Cudahy, T. J., Mizuhiko, S., Ueda, K., & Mauger, A. j. (2005). Seamless geological map generation using ASTER in the Broken Hill-Curnamona province of Australia. Remote Sensing of Environment, 99: 159-172.

[53] Grove, C. I., Hook, S. J. & Paylor III, E. D. (1992). Laboratory reflectance spectra of 160 minerals,0.4 to 2.5 micrometers.

[54] Hunt, G. R. & Salisbury, J. W. (1971). Visible and near infrared spectra of minerals and rocks. II. Carbonates. Modern Geology, 2, 23-30.

[55] Salisbury, J. W. & D'Aria, D. M. (1992). Emissivity of terrestrial materials in the 8–14 μm atmospheric window. Remote Sensing of Environment, 42(2), 83-106.

[56] Vicente, L. E. & de Souza Filho, C. R. (2011). Identification of mineral components in tropical soils using reflectance spectroscopy and advanced spaceborne thermal emission and reflection radiometer (ASTER) data. Remote Sensing of Environment, 115(8), 1824-1836.

[57] El-Qassas, R. A. Y., Abu-Donia, A. M., & Omar, A. E. A. (2023). Delineation of hydrothermal alteration zones associated with mineral deposits, using remote sensing and airborne geophysics data. A case study: El-Bakriya area, Central Eastern Desert, Egypt. Acta Geodaetica et Geophysica, 5, 71–107.

[58] Shahi, H., & Kamkar-Rouhami, A. (2014). A GIS-based weights of evidence model for mineral potential mapping of hydrothermal gold deposits in Torbat-e-Heydarieh area. Journal of Mining and Environment, 5(2), 79-89.

[59] Mhangara, P. (2005). Testing the ability of ASTER (Advanced spaceborne thermal emission and reflection radiometer) to tap hydrothermal alteration zones: a case study of the Haib Porphyry Copper-Molybdenum Deposit, Namibia. MSc dissertation, Stellenbosch University. [1]. Munoz, G., Exploring for geothermal resources with electromagnetic methods. Surveys in geophysics, 2014. 35(1): p. 101-122.